

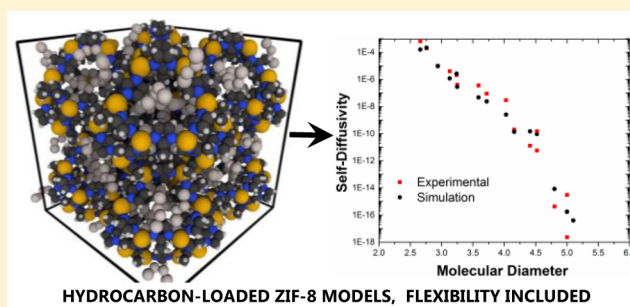
Temperature and Loading-Dependent Diffusion of Light Hydrocarbons in ZIF-8 as Predicted Through Fully Flexible Molecular Simulations

Ross J. Verploegh, Sankar Nair, and David S. Sholl*

School of Chemical & Biomolecular Engineering, Georgia Institute of Technology, Atlanta, Georgia 30332-0100, United States

S Supporting Information

ABSTRACT: Accurate and efficient predictions of hydrocarbon diffusivities in zeolitic imidazolate frameworks (ZIFs) are challenging, due to the small pore size of materials such as ZIF-8 and the wide range of diffusion time scales of hydrocarbon molecules in ZIFs. Here we have computationally measured the hopping rates of 15 different molecules (kinetic diameters of 2.66–5.10 Å) in ZIF-8 via dynamically corrected transition state theory (dcTST). Umbrella sampling combined with the one-dimensional weighted histogram analysis method (WHAM) was used to calculate the diffusion free energy barriers. Both the umbrella sampling and dynamical correction calculations included ZIF-8 flexibility, which is found to be critical in accurately describing molecular diffusion in this material. Comparison of the computed diffusivities to extant experimental results shows remarkable agreement within an order of magnitude for all the molecules. The dcTST method was also applied to study the effect of hydrocarbon loadings. Self and transport diffusion coefficients of methane, ethane, ethylene, propane, propylene, *n*-butane, and 1-butene in ZIF-8 are reported over a temperature range of 0–150 °C and loadings from infinite dilution to liquid-like loadings.



1. INTRODUCTION

New separation strategies for light paraffin and olefin species that have small differences in relative volatilities could have a significant industrial impact.¹ Currently, the industry standard for olefin/paraffin separations is cryogenic distillation, with approximately 85% of the annual operating cost attributed to energy consumption.² One class of proposed alternative processes uses nanoporous materials as adsorbents in thermodynamically controlled pressure, temperature, and (or) vacuum swing adsorption separations or as size-selective entities in kinetically controlled membrane or adsorption separations.³ Regardless of the choice between a thermodynamic or kinetic separation process, it is necessary to know the diffusion coefficients of hydrocarbons in the nanoporous material of choice to accurately design the separation process.

Metal–organic frameworks (MOFs) are a class of nanoporous materials formed through coordination bonds between metal centers and organic linkers.⁴ MOFs have many proposed uses such as gas storage, catalysis,⁵ chemical sensing,⁶ drug delivery,⁷ and chemical separations⁸ and their ordered pore networks lend themselves to study by molecular simulations.⁹ Considerable experimental work has focused on exploiting the molecular sieving characteristics of ZIF-8, a prototypical small pore MOF.^{10,11} ZIF-8 is water stable, thermally stable up to 550 °C, demonstrates permanent porosity, and is easily synthesized.¹² ZIF-8 has been experimentally shown to exhibit interesting sieving properties with regard to increasing hydrocarbon chain length and morphology.¹³ Specifically,

ZIF-8 has shown a sharp kinetic separation between propylene and propane with single-component and binary permeation selectivities in a range of 15 to 60 at room temperature and 35 °C.^{14–17} Pan and Lai demonstrated not only a sharp C₃ olefin/paraffin separation but also a promising ideal C₂/C₃ permeation separation of 6.6 at 1 bar and 298 K.¹⁸ Furthermore, Bux and co-workers showed permeation selectivities of 2.4 for ethylene over ethane for an equimolar bulk gas mixture at room temperature and 6 bar with a ZIF-8 membrane.¹⁹

Previous simulation studies of molecular diffusion in ZIF-8 have focused on relatively fast diffusing small molecules such as hydrogen,²⁰ noble gases,²¹ carbon dioxide,²² and small alcohols²³ using both rigid and flexible ZIF-8 frameworks. Diffusion coefficients of such rapidly diffusing species can be calculated in nanoporous materials through straightforward equilibrium molecular dynamics (EMD) simulations.²⁴ Unfortunately, many of the hydrocarbon species of interest in ZIF-8 have diffusivities lower than 10^{−12} m²/s, which are high enough to be of industrial relevance but too low to measure with EMD. To date, only one simulation study has attempted to demonstrate the hydrocarbon sieving properties of ZIF-8. Zheng et al. simulated the self-diffusion of methane, ethane, ethylene, and propane and made a comparison to transport diffusivities experimentally measured using the Wicke-Kallen-

Received: August 18, 2015

Published: November 25, 2015

bach (WK) technique.²⁵ Their results for propane show poor convergence because of the slow hopping of propane in ZIF-8 on molecular dynamics (MD) time scales. To circumvent this time-scale dilemma, the diffusion of adsorbates may be considered as an activated hopping process of an adsorbate between low energy regions.²⁶ Within this description, enhanced sampling methods such as transition path sampling or dynamically corrected transition state theory (dcTST) can be applied to characterize the diffusion properties of slowly diffusing adsorbates.^{26–38}

MOFs also exhibit a variety of flexible phenomena such as intraframework dynamics, swelling, negative thermal expansion, gate opening, and breathing.³⁹ By Coudert's classification,³⁹ ZIF-8 displays intraframework dynamics through methylimidazole (mIm) organic linker rotation. The swinging of the mIm organic linker is caused by both thermal fluctuations, as shown by ab initio MD calculations (AIMD),^{40,41} and forces exerted by adsorbed molecules, as shown by Fairen-Jimenez using in situ powder X-ray diffraction (XRD).⁴² The latter phenomenon generates a thermodynamically metastable structure with a larger window diameter (3.81 Å) than the empty ZIF-8 structure (3.42 Å).⁴² Uptake experiments and single-component breakthrough measurements have shown that ZIF-8 accepts chemical species (e.g., isobutane, benzene, xylene isomers, and 1,2,4-trimethylbenzene) that have kinetic diameters larger than ZIF-8's measured powder XRD pore size (3.42 Å).^{13,43,44} Haldoupis and co-workers demonstrated using a combination of AIMD and TST simulations that it was essential to include thermal intraframework motions in predicting methane diffusion in ZIF-8.⁴⁰ The simulated diffusion coefficient of methane in the rigid ZIF-8 structure is not measurable by standard EMD. The approximate procedure by Haldoupis et al. of thermally averaging the hopping rate over a set of structures predicts a larger diffusion coefficient than that measured in the rigid structure. This is consistent with the results of Hertäg et al., who also demonstrated that inclusion of ZIF-8 framework flexibility in EMD simulations was critical in accurately describing methane mobility.²⁰ The methods used by Haldoupis et al. do not account for coupling between the diffusing molecule and the ZIF framework.

In this study, we have simulated the self and transport diffusivities of methane, ethane, ethylene, propane, propene, *n*-butane, and 1-butene in ZIF-8 over industrially relevant temperature and loading ranges using molecular simulation techniques that incorporate ZIF-8 intraframework motions and compared our results to reported experimental results. We begin by briefly discussing the theory behind the calculation of diffusivities as well as define the simulation methods and force fields used in our calculations. The dcTST methodology was then applied to a range of adsorbed species in ZIF-8 and the computed diffusivities are compared to experimental data. We also describe the loading dependence of the self and transport diffusion coefficients of alkanes and alkenes in ZIF-8 and use this information to predict hydrocarbon permeabilities through a ZIF-8 membrane.

2. THEORY

2.1. Diffusion Background. Fick's law describes macroscopic transport by combining a single-component transport diffusivity with a concentration gradient as the driving force.²⁴ Molecular simulations can be used to calculate self-diffusion coefficients, $D_{\text{self},i}$ as well as collective (corrected) diffusion coefficients, $D_{0,i}$ where the subscript i indicates the molecular

species.^{24,45} Self and collective diffusion coefficients are correlated through the following sum of parallel resistances:⁴⁶

$$1/D_{\text{self},i} = 1/D_{0,i} + 1/D_{i,i} \quad (1)$$

where $D_{i,i}$ is the Maxwell–Stefan self-exchange diffusivity. MOFs exhibiting one-, two-, or three-dimensional topologies, small pore limiting diameters (PLDs), and large cavities have the most potential for molecular sieving based applications. Small pore diameters allow for molecular sieving of molecules with different molecular diameters and large cavities allow for mixing of species within the cavities. Below, we assume that correlated mixing effects are negligible in cage-type frameworks with large cages and small windows.^{46,47} Therefore, it is possible to assume for unary loadings that the Maxwell–Stefan self-exchange diffusivity is large and can be neglected. This means that $D_{\text{self},i} = D_{0,i}$ at any unary loading and the relationship between the transport diffusivity $D_{T,i}$ and the self-diffusivity, known as Darken's equation, can then be written as:⁴⁶

$$D_{T,i} = D_{\text{self},i} (\partial \ln p / \partial \ln c) \quad (2)$$

The quantity in parentheses is known as the thermodynamic correction factor where c is the adsorbate loading and p is the corresponding pressure. The thermodynamic correction factor is derived from an adsorption isotherm, calculated either with grand canonical Monte Carlo (GCMC) simulations or measured experimentally. In general, both the transport and self-diffusivities are functions of loading and temperature.

We also assume that the diffusion of adsorbates through a cage-type material can be viewed as an activated hopping process.²⁶ The loading-dependent self-diffusivity can then be written as a function of the loading-dependent overall exit hopping rate:

$$D_{\text{self},i} = \frac{1}{2n} k_{A \rightarrow \text{ALL}}^{\text{EXIT}} \lambda^2 \quad (3)$$

where λ is the distance between low energy sites and n can take on values of 1, 2, or 3 depending on the dimensionality of diffusion. For ZIF-8, $n = 3$. The exit hopping rate in the expression above is the sum of the hopping rates over all windows exiting a cage.

2.2. Calculating the Diffusion Hopping Rate at Infinite Dilution. Transition state theory (TST) is applicable to describing processes that are characterized by sequences of rare events such as the hopping of adsorbates from cage to cage in ZIF-8.^{48,49} To apply TST, one must have a method that efficiently explores the free energy landscape and locates at least approximately the location of a transition state. These methods include, but are not limited to, the nudged elastic band (NEB) method,⁵⁰ biased sampling methods such as umbrella sampling (US),^{51,52} temperature accelerated dynamics (TAD),⁵³ steered molecular dynamics (SMD),⁵⁴ metadynamics,⁵⁵ Monte Carlo (MC) histogramming methods,⁵⁶ and path sampling methods such as transition path sampling (TPS)⁵⁷ and transition interface sampling (TIS).⁵⁸ Each method utilizes different simplifying assumptions and can be combined with a variety of approaches to calculate free energies. For example, the NEB method neglects the entropic contribution to the hopping rate yielding only the minimum potential energy barrier. SMD can be combined with thermodynamic integration⁵⁹ to yield free energies from the force required to undergo a transition between two metastable microstates. US and MC histogramming both require an a priori definition of a reaction coordinate

(RC) upon which to map the free energy directly from probabilities. Path sampling methods do not require definition of a reaction coordinate or calculation of a transmission coefficient but can be computationally expensive.³⁵

Within TST, the assumption is made that all systems that reach the transition state (TS) starting from one free energy minimum position (state A) will thermalize in the other free energy minimum position (state B) of interest. For consistency, we will refer to the system as the diffusing adsorbate and ZIF-8 atoms that comprise the window region, state A as the exiting cage, and state B as the receiving cage. TST's treatment of the rate typically overestimates the effective rate by neglecting rapid recrossing events. These recrossings are consequences of the adsorbate having a high kinetic energy after the initial crossing, the geometry of the adsorbent around the TS, or the presence of other adsorbates.^{37,60} To correct for this phenomena, it is possible to multiply the TST derived rate by the dynamical correction (dc) factor or transmission coefficient.⁶¹ The transmission coefficient is defined as the probability that the system (the adsorbate) will thermalize within state B (receiving cage) from a trajectory starting at the TS. For a single Lennard–Jones (LJ) fluid (spherical) adsorbate in rigid frameworks at infinite dilution where the transition state is known exactly, the transmission coefficient is typically close to unity. However, this dynamical correction becomes non-negligible for more complex adsorbates, higher adsorbate loadings, and situations such as the presence of a flexible framework where an imperfect reaction coordinate means that the TS dividing surface is not known exactly.

2.3. Coupling of Adsorbate and MOF Framework Motions. Adsorbates with kinetic diameters larger than the pore limiting diameter of ZIF-8 have been clearly demonstrated experimentally to diffuse inside ZIF-8.^{13,43,44} This can potentially occur due to flexibility inherent in the ZIF-8 windows or due to deformations of the windows induced by adsorbed molecules. It is not unreasonable to consider that during a crossing event, a large adsorbate would effectively brace the window open. The existing literature modeling diffusion in ZIF-8 has not examined the latter effect. Previous simulation studies have considered the effect of framework flexibility on diffusion of spherical adsorbates by assuming a decoupling of framework motions from the hopping trajectory of the adsorbate. Haldoupis et al. and Awati et al. have utilized methods to measure histograms of window sizes in empty ZIF-8⁴⁰ and zeolite frameworks^{62,63} respectively. In these calculations, only the equilibrium framework motions of the empty (nonloaded) structures are considered. Recent work by Boulfelfel et al. has shown that this approach neglects important adsorbate-induced deformation during diffusion of extended hydrocarbons in small pore zeolites.⁶⁴ To accurately describe diffusion of the broadest range of molecules inside ZIF-8, it is important to adopt methods that incorporate all the coupled adsorbate-framework degrees of freedom (DOF).

2.4. Loading Dependence of the Diffusion Coefficient. Extending the free energy methods described above to higher loadings has been attempted in only a small number of studies. Tunca and Ford were the first to extend TST to describe high loading diffusion of spherical molecules in nanoporous crystals.^{56,65,66} Dubbeldam and co-workers extended dcTST to higher loading alkane diffusion in rigid zeolites.³⁷ Beerdsen and co-workers studied the loading dependence of methane diffusion in rigid cage-, channel-, and intersecting-type zeolites.⁶⁷ Jee et al. simulated methane/carbon dioxide mixtures

in silica zeolite DDR and demonstrated excellent agreement between MD and TST-kinetic Monte Carlo (KMC) methods.⁶⁸ Recently, Smit and co-workers followed the TST-KMC approach of Jee et al. in order to calculate the collective (corrected transport) diffusivity of methane in zeolite Si-LTA with excellent agreement to EMD simulations.⁶⁰ In all of these studies, one adsorbate molecule was tracked while all other adsorbates, even those in the exiting and receiving cages, were treated as a contributing background potential.

In this study, we propose a simplified scheme that assumes the self-diffusion coefficient is a function of only symmetric receiving and exiting cage loadings. Asymmetric cage loadings are not taken into account as they are in the work by Smit and co-workers.⁶⁰ The results of Dubbeldam et al. and Jee et al. demonstrated that specific loadings in surrounding cages do not have a strong effect on the local hopping rates in cage-type materials.^{37,68} More careful treatment of asymmetric loadings may be justified if high precision information on loading-dependent diffusivities is required in a specific example. It is important to clarify that all the studies of loading-dependent diffusion mentioned above treated the nanoporous framework as rigid. Below, we extend these methods to include framework flexibility. A recent study by Theodorou and co-workers applied umbrella sampling to study infinite dilution benzene diffusion in fully flexible silicalite at three temperatures.⁶⁹ To our knowledge, no prior studies have been performed that apply dcTST to investigate the loading-dependent transport properties of adsorbates within fully flexible MOFs.

3. COMPUTATIONAL METHODS

3.1. ZIF-8 and Adsorbate Force Fields. ZIF-8 has been experimentally shown to undergo a low loading (LL) to high loading (HL) structural transition upon adsorption of N₂ at 77 K.⁴² This transition is associated with the rotation of the linkers about the N–N axis of the imidazole ring.²⁵ A force field (FF) developed by Zhang and co-workers was parametrized to reproduce the ZIF-8 LL to HL transition using a hybrid Gibbs Ensemble MC and NPT-MD simulation.⁷⁰ The force field of Zhang et al. was used to describe the ZIF-8 framework in our calculation. The starting ZIF-8 crystallographic structure for all the simulations was obtained from the Cambridge Structural Database (structure code OFERUN).^{71,72}

The TraPPE united atom force field was applied to describe adsorbate–adsorbate interactions for methane, ethane, ethylene, propane, propylene, *n*-butane, 1-butene, isobutane, and isobutene.^{73,74} The bonds in these molecules were considered to be flexible⁷⁵ and charges were not considered. In addition to hydrocarbons, the following small adsorbates were also considered: He, SF₆, H₂, N₂, O₂, and CO₂. He was described as a single-site 12–6 LJ fluid.⁷⁶ SF₆ was also described as a single-site 12–6 LJ fluid.⁷⁷ H₂ was described by the Michels-Degraaff-Tenseldam model with charges from the Darkim–Levesque model and a fixed H–H bond length of 0.741 Å.⁷⁸ N₂ was described by the TraPPE FF with a fixed N–N bond length of 1.100 Å.⁷⁹ The LJ parameters for N₂ were taken directly from Zhang et al.⁷⁰ and are slightly different than the parameters reported from Potoff and Siepmann.⁷⁹ O₂ was described by the TraPPE FF with a fixed O–O bond length of 1.210 Å.⁸⁰ CO₂ was described by the rigid EPM2 FF with a fixed C–O bond length of 1.160 Å.⁸¹ H₂, N₂, O₂, and CO₂ were modeled as rigid molecules. All adsorbate FF parameters can be found in the [Supporting Information](#).

All calculations were carried out in 2 × 2 × 2 ZIF-8 unit cell simulation volume with periodic boundary conditions (PBCs). Lorentz–Berthelot mixing rules described all adsorbate–framework 12–6 LJ interactions in both MC and MD simulations. Lennard–Jones potential interactions were truncated at a spherical radius of 16.5 Å and analytical tail corrections were applied. Ewald summation was used to compute long-range Coulombic interactions with a desired

relative error in forces of 10^{-6} . In every case, the simulation volumes used were charge neutral.

3.2. Grand Canonical Monte Carlo. GCMC calculations were performed using RASPA to measure adsorption isotherms in ZIF-8.⁸² ZIF-8 was modeled as a rigid structure with the energy minimized structure given by the Zhang FF in these calculations. Park et al. reported a LL ZIF-8 structure, determined by XRD at 258 K and 1 atm, with unit cell parameters of $a = b = c = 16.991 \text{ \AA}$.¹² Unit cell parameters for the LL FF minimized ZIF-8 structure were $a = b = c = 16.991 \text{ \AA}$. The HL form of ZIF-8 as reported by Fairen-Jimenez has unit cell parameters of $a = b = c = 17.107 \text{ \AA}$.⁴² Our HL ZIF-8 FF minimized structure has unit cell parameters of $a = 17.09 \text{ \AA}$, $b = 17.16 \text{ \AA}$, and $c = 17.07 \text{ \AA}$. These minor differences in lattice parameters have a negligible effect on the adsorption of hydrocarbons. Pretabulated energy and Coulombic grids were generated with a 0.1 \AA spacing to enhance computational efficiency. Further simulation details can be found in the [Supporting Information](#).

3.3. Free Energy Mapping. Umbrella sampling was chosen as the biased sampling method. To implement umbrella sampling, a one-dimensional RC was chosen that starts in cage A, passes through the narrow window, and ends in cage B. The window region is loosely defined as a geometric plane in the center of the 6 member ring of ZIF-8. In flexible structures this plane is a $3N-1$ -dimensional surface where N is the number of atoms and the position of which is time-varying. Any reference to the TS location with the one-dimensional RC is therefore an approximate description of the true TS. The RC is defined by the vector between the geometric centers of cage A and cage B. [Figure 1](#) shows a schematic of ZIF-8 and an idealized representation of how umbrella sampling is performed.

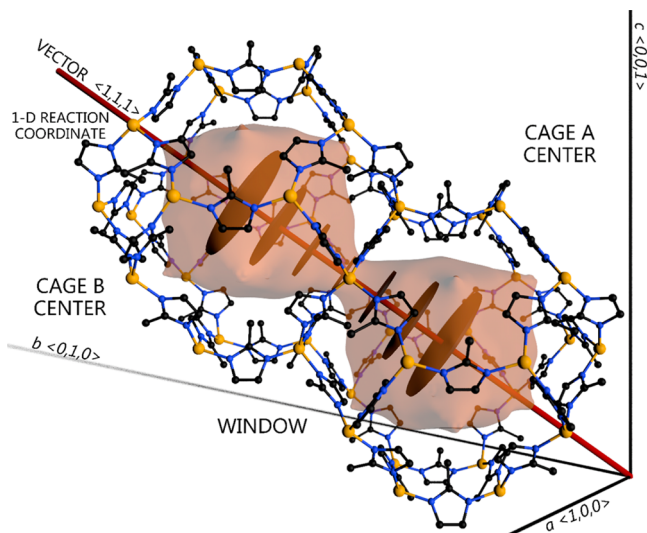


Figure 1. Schematic of the linear reaction coordinate (red vector) traversing the window between two ZIF-8 cages. Umbrellas are idealized as brown discs on the red 1-D RC. The other 14 cages in the $2 \times 2 \times 2$ ZIF-8 simulation volume as well as hydrogen atoms have been removed for clarity. Spheres colored in yellow, blue, and black correspond respectively to Zn, N, and C atoms.

All NVT EMD simulations were performed using LAMMPS.⁸³ The velocity-Verlet integration algorithm was used with a 1 fs time step. For NVT simulations, a Nose–Hoover thermostat was applied with a temperature damping parameter of 100.0 fs . The framework lattice constants and atomic positions were optimized prior to each idealization using the Zhang FF. The conjugate gradient (CG) algorithm as implemented in LAMMPS was used to anisotropically relax both the unit cell parameters and atomic positions. A second minimization step involved using a Hessian-free truncated Newton–Raphson algorithm to relax only the atomic positions. Both minimization steps adhered to a force cutoff of $0.231 \text{ kcal/mol \AA}^2$.

The velocities of all atoms were then initialized from a Maxwell–Boltzmann distribution representative of the specified temperature.

The collective variables (colvars) package developed by Fiorin and co-workers was utilized within LAMMPS to perform the umbrella sampling calculations.⁸⁴ During umbrella sampling, an adsorbate is constrained to a 3-D region orthogonal to the reaction coordinate by a spring. The larger the spring constant, the thinner the 3-D region is, with thinner regions requiring more overlapping umbrella simulations. For faster moving adsorbates (He, H₂, N₂, CO₂), a spring constant of $10 \text{ kcal mol}^{-1} \text{ \AA}^{-1}$ was used. A spring constant of $25 \text{ kcal mol}^{-1} \text{ \AA}^{-1}$ was used for the O₂, methane, ethane, ethylene, propane, propylene, *n*-butane, and 1-butene simulations. For both these sets of adsorbates, simulations utilized 30 umbrellas with an approximate spacing of 0.508 \AA . Isobutane, isobutene, and SF₆ simulations used a spring constant of $150 \text{ kcal mol}^{-1} \text{ \AA}^{-1}$, with 50 umbrellas each having an approximate spacing of 0.301 \AA . For adsorbates with multiple DOFs, the constraining harmonic potential was applied to the molecule's center of mass (COM). A 100 ps equilibration simulation was performed before the $250\text{--}500 \text{ ps}$ production period for each umbrella. Adsorbates with more DOFs required longer production runs for efficient sampling. The weighted histogram analysis method (WHAM) was utilized to combine the different umbrella simulations into a free energy curve.⁸⁵

In simulations with the smaller adsorbates, we found that the tracked adsorbate was able to hop to another cage if the umbrella plane was positioned orthogonal to another ZIF-8 window. This led to poor sampling of the specified microstates. Using a Monte Carlo histogramming method (e.g., Awati et al.⁶²), the integral over the free energies associated with those microstates of interest is calculated to determine a hopping rate; likewise, only the likelihood of molecular positions within this localized region should be sampled when performing umbrella sampling. For example, if a plane is placed parallel to the window region, one finds that the plane dissects the center of neighboring cages. Sampling these low energy regions would predict a much lower energy barrier when combining umbrella simulations with WHAM. To constrain faster moving adsorbates to the specified cage, a blocking potential (repulsive spherical wall) was created around the cage with a radius of 9 \AA . Any tracked adsorbate exiting the microstate experienced a repulsive harmonic potential with a force constant of $200 \text{ kcal/mol \AA}^2$ when approaching within 1 \AA of the spherical wall. No other atoms within the simulation were subjected to this artificial blocking potential. The total potential energy of the system was analyzed to detect unrealistic spikes that would indicate high forces and therefore, corresponding unphysical velocities. Unwanted adsorbate hopping only occurred one or two times during specific umbrella simulations and we concluded that the brief sampling of these high energy regions had a negligible effect on the final free energy curve.

3.4. Transmission Coefficient Calculation. Transmission coefficients were calculated using the procedure described by Frenkel and Smit.⁴⁸ To begin, an ensemble of starting configurations of the adsorbate at the TS must be recorded. We used an umbrella sampling simulation during which the tracked adsorbate is held fixed by a tight spring of $1000 \text{ kcal mol}^{-1} \text{ \AA}^2$ to a plane orthogonal to the TS RC. A 100 ps equilibration simulation is performed before 1000 snapshots are recorded with a sampling frequency of 0.25 ps . A starting snapshot for each trajectory was chosen from the 1000 snapshots using a uniform distribution. Before running the short MD simulations, the velocities of all atoms, both adsorbate and framework, are randomized according to the Maxwell–Boltzmann distribution at the specified temperature. Each trajectory was run for a total of 6 ps , 3 ps backward and forward in time. Through trial and error, this length was found to be sufficient for the transmission coefficient curves to reach a plateau. The adsorbate COM distance from the TS barrier was tracked to determine whether it was in the exiting or receiving cage. A minimum of 1500 trajectories were gathered for the reported transmission coefficients.

3.5. Methods for Measuring Loading-Dependent Self-Diffusivities. The simulation method for measuring loading-dependent self-diffusivities is almost identical to the description of free energy

mapping and calculation of the transmission coefficient at infinite dilution. In both calculations, only one adsorbate is tracked. All the extra adsorbates are considered simply as a background potential. A fixed number of adsorbate molecules are added to the system using Widom insertion as implemented in RASPA. The number of molecules placed in both the exiting and receiving cages is set to the total number of adsorbates in the simulation volume divided by the number of ZIF-8 cages (16 cages for the $2 \times 2 \times 2$ simulation volume). An adsorbate is then randomly chosen from the other adsorbates not in the receiving or exiting cages, and its coordinates are set approximately at the TS region between the exiting and receiving cages. This adsorbate becomes the tracked adsorbate. Placing the tracked adsorbate at the TS at the beginning of the simulation ensures that the tracked adsorbate does not initially overlap with any other adsorbates and allows for a smooth relaxation into the appropriate cage based on the location of the spring. All other simulation details are the same as described in Section 3.3.

4. RESULTS AND DISCUSSION

4.1. Infinite Dilution: Hydrocarbons in ZIF-8. Figure 2 shows representative free energy curves of propane at infinite

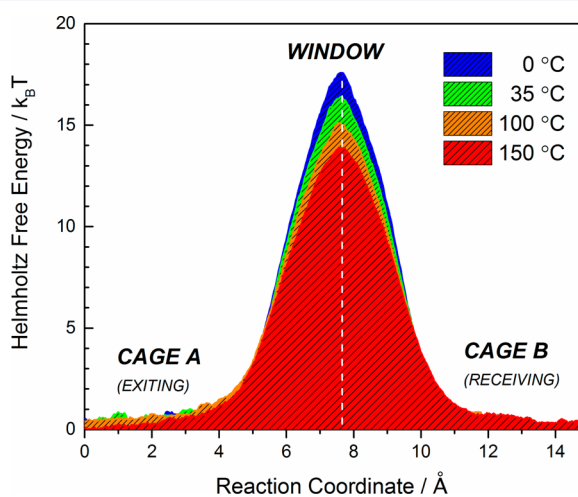


Figure 2. Free energy curves for propane at infinite dilution as a function of temperature in flexible ZIF-8.

dilution in ZIF-8. The free energy curves for other adsorbates are similar and several examples are reported in the Supporting Information. RC values of 0 and 14.72 Å correspond to the center of the exiting cage and the receiving cage, respectively. The TS is located at approximately 7.6 Å on the RC. This value was used to generate trajectories for the transmission coefficient calculations.

Figure 3 shows how the transmission coefficient curves for propane vary with respect to time. In general, the transmission coefficient increases as temperature is increased. At 35 °C and infinite dilution, transmission coefficients for the 15 adsorbates ranges from 0.843 to 0.025 as reported in Table S5 of the Supporting Information. Generally, adsorbates with smaller kinetic diameters such as He, H₂, N₂, and O₂ have transmission coefficients closer to 1. Isobutane and isobutene have the lowest transmission coefficients. Dubbeldam et al. reported transmission coefficients for propane in a rigid model of zeolite LTL around 0.5 at 300 K and infinite dilution.³⁷ This is comparable to our result for propane shown in Figure 3 for flexible ZIF-8. Abouelnasr et al. reported a transmission coefficient of almost unity for methane in rigid LTA-type zeolite at 300 K.⁶⁰

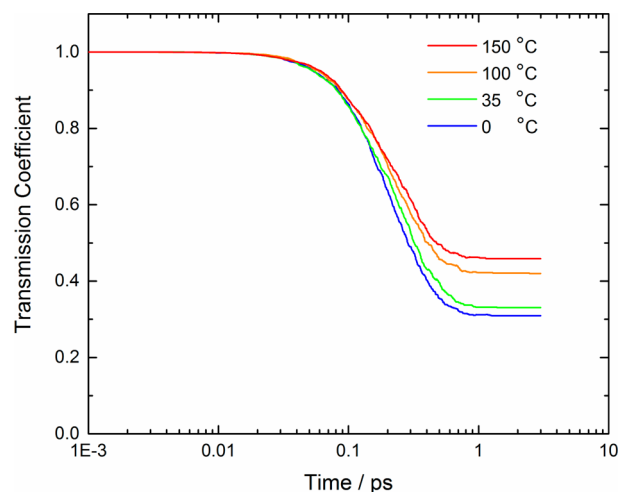


Figure 3. Transmission coefficient curves for propane at infinite dilution in flexible ZIF-8 as a function of time for various temperatures.

Our computed infinite-dilution diffusivities for 15 molecules at 35 °C are shown in Figure 4. The self-diffusivities at 0, 35, 100, and 150 °C, along with diffusion activation energies predicted through an Arrhenius fit, are reported in Table S6 of the Supporting Information. The diffusion activation energies increase roughly linearly ($R^2 = 0.875$) as a function of increasing molecular diameter. For the linear hydrocarbons, the greatest differences in the activation energies occur between C₂/C₃= (5.4 kJ/mol) and C₃=/C₃ (4.7 kJ/mol), supporting experimental claims that ZIF-8 can be used to kinetically separate these species. A key observation from Figure 4 is that the methods we have used here give results for a range of diffusivities that greatly exceeds what is possible with standard MD calculations. The slowest diffusing species we examined, SF₆, diffuses 9–10 orders of magnitude more slowly than can be observed with simple MD. The large range of diffusivities than can be assessed with the methods we have used makes it possible for the first time to compare computed diffusivities in ZIF-8 to experimental data in a comprehensive way.

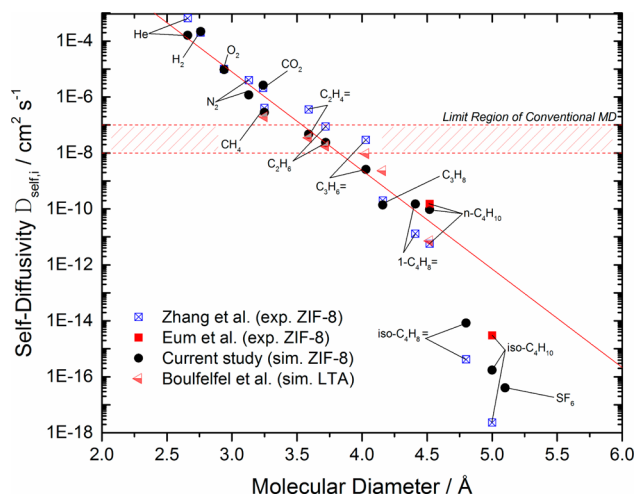


Figure 4. Infinite-dilution self-diffusion coefficients for small non-spherical molecules and light key hydrocarbons at 35 °C as a function of molecular diameter. Experimental data was taken directly from Zhang et al.¹³ and Eum et al.⁸⁶ Simulated C₁–C₄ diffusivities in LTA zeolite taken from Boulfefel et al.⁶⁴

Figure 4 shows a comparison between the experimentally measured diffusion data from Zhang and co-workers and our simulated self-diffusivities at infinite dilution and 35 °C. Zhang and co-workers collected data using two different methods: (1) kinetic uptake with a pressure decay cell for adsorbates diffusing slower than 10^{-8} cm² s⁻¹ and (2) mixed-matrix membrane permeation for faster diffusing species.¹³ The overall agreement between the experimental and simulated results is excellent, with the simulation results for each adsorbate lying within an order of magnitude of the experimental results. There are some quantitative differences between the computed and experimental results. For example, Zhang et al. predicted the ideal diffusion selectivity, defined as the ratio of the self-diffusion coefficients, of propylene over propane to be 145, while our calculations predict this ratio to be 19. Pressure decay cell diffusion data from Eum et al. for *n*-butane and isobutane in ZIF-8 has also been included in Figure 4.⁸⁶ The difference between the data by Eum et al. and Zhang et al. highlights the observation that measuring slow diffusion in materials of this kind experimentally can be challenging. It also points to the risks associated with drawing overly strong conclusions about the accuracy (or inaccuracy) of computational predictions based on comparisons with a single experimental measurement.

It is interesting to compare our results for ZIF-8 with data from similar calculations in small pore zeolites. Figure 4 includes results from recent calculations by Boulfefel et al.⁶⁴ for C₁–C₄ hydrocarbons in Si-LTA. The PLD of this silica zeolite (ITQ-29), defined using Zeo++ with atomic radii of 1.35 Å for both Si and O atoms,⁸⁷ is 3.995 Å,⁸⁸ so the window size in Si-LTA is comparable to the window size of ZIF-8 (3.42 Å). Surprisingly, the computed diffusivities in Si-LTA follow the trend observed in our calculations for ZIF-8 with almost quantitative accuracy. In both materials, flexibility of the windows is critical to diffusion; that is, calculations using rigid structures yield vastly lower diffusivities. It is conventional to think of zeolites as “more rigid” than MOFs. The data in Figure 4 suggest that at least in this example, carrying this concept to its logical conclusion would lead to incorrect predictions for the trend in diffusion for adsorbates as a function of size.

The red line in Figure 4 shows a linear fit to our simulated diffusivities for the species with kinetic diameters less than 4.5 Å. Our linear fit assumes that the reported molecular diameters best represent the true morphology of the molecules presented in this study. This assumption captures the overall trend among the different molecules well, although there are clearly examples such as N₂, CO₂, and CH₄ where this simple trend is not adequate to completely describe the data. Molecules with kinetic diameters larger than 4.5 Å diffuse much more slowly than would be suggested by this empirical linear fit.

It is useful to consider whether the adsorbates passing through windows in ZIF-8 affect the window size. Intuitively, it seems possible that adsorbates, especially those with extended geometries, may be able to brace the window open while they are close to the dividing surface. Figure 5 shows the observed window size distributions when an adsorbate is constrained by a harmonic spring at the dividing surface defined above. Snapshots from the starting configurations used to compute transmission coefficients were used for this analysis. Using the same window diameter finding algorithm of Haldoupis and co-workers⁴⁷ and the percolation algorithm of Ziff and Newman,⁸⁹ the window diameter of the relevant window was determined for each configuration. Grid based percolation methods underestimate the true window diameters, unlike methods

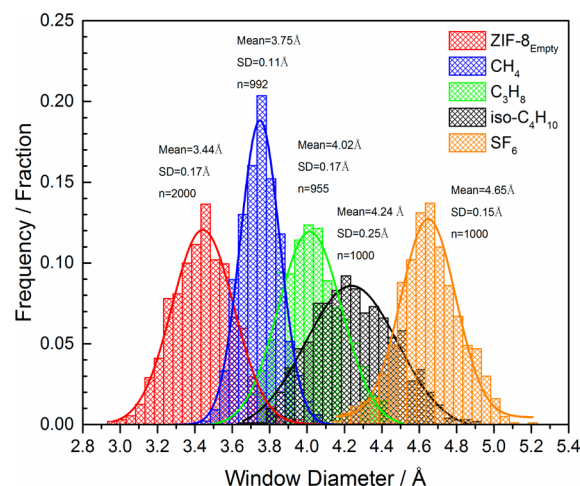


Figure 5. ZIF-8 window size distributions at 35 °C for configurations with adsorbates constrained to be in the window as described in the text.

that yield graph representations of the void space through Voronoi decomposition (Zeo++).⁸⁷ When using a specific grid spacing in a grid based method, one can more accurately determine the true window diameter using

$$D_w = D_{w,\text{grid}} + \sqrt{3} d_{\text{grid}} \quad (4)$$

where D_w is the true window diameter, $D_{w,\text{grid}}$ is the window diameter measured at a particular grid spacing, and d_{grid} is the grid spacing. The factor of $\sqrt{3}$ is derived from geometric arguments based on an imperfect three-dimensional grid placement. Using eq 4, we compared grid based PLD measurements at grid spacings of 0.1 and 0.25 Å for the experimentally reported ZIF-8 structures (structure codes VELVOY and OFERUN) to those predicted by Zeo++ and found differences of no greater than 0.028 Å. We therefore used eq 4 with a grid spacing of 0.25 Å for computational efficiency in the calculations reported below. The average window diameter of 3.44 ± 0.17 Å in the empty ZIF-8 structure calculated using the Zhang FF agrees well with the AIMD derived window diameter of 3.41 ± 0.16 Å reported by Haldoupis et al.⁴⁰

Figure 5 shows there is a considerable overlap between the window sizes seen in the empty framework and those seen when CH₄ is constrained to be in the window. This suggests that even without including the influence of CH₄ on the ZIF-8 window, configurations occur that allow CH₄ to hop through the window. This concept is central to earlier approximate calculations by Haldoupis et al. for ZIF-8⁴⁰ and Awati et al. for eight member ring zeolites^{62,63} that use a collection of snapshots from an empty structure to estimate the impact of framework flexibility on diffusion. For the larger molecules shown in Figure 5, however, there is almost no overlap between the window size distribution of the empty framework and the configurations with molecules constrained in the window. For SF₆, for example, the window diameters three standard deviations above the mean for the empty framework (3.95 Å) and three standard deviations below the mean for the configurations including SF₆ (4.20 Å) are separated by 0.25 Å. It is clear from this gap that calculations that ignore coupling between adsorbates and the framework DOFs will not be able to give accurate diffusion coefficients for large molecules of this kind.

It is important to note that the diffusion of the largest molecules in Figure 5 is not associated with a structural transition of ZIF-8 from the LL to HL structure discussed above. We present evidence below that hydrocarbon adsorption in ZIF-8 near room temperature does not promote this transition. Even if ZIF-8 did convert to the HL structure upon adsorption of large molecules, the pore size of this structure is still considerably smaller than the values observed in Figure 5 for the largest diffusing species: Zeo++ yields a PLD of 3.35 (3.88) Å in the FF energy minimized LL (HL) structure and the HL structure reported by Fairen-Jimenez et al.⁴² has a PLD of 3.81 Å.

4.2. Loading Dependence of Hydrocarbon Diffusion in ZIF-8. The self-diffusion coefficients of hydrocarbons in cage-type MOFs are a function of loading and understanding this loading dependence is necessary in determining optimal separation conditions. One issue not addressed in the current literature is whether the ZIF-8 framework adopts the HL form upon adsorption of hydrocarbons at 35 °C. This LL to HL transition, as evident through a stepped isotherm, has not been observed experimentally for hydrocarbon adsorption.¹³ Duren and co-workers, however, concluded from simulated adsorption of C₂–C₄ paraffins in LL and HL structures of ZIF-8 at 0 °C that experimental adsorption data qualitatively fit the simulated LL (HL) structure isotherm well at low (high) pressures.⁹⁰ To resolve this question, calculations that establish the thermodynamic stability of the LL and HL structures in the presence of adsorbed species are needed. Osmotic framework adsorbed solution theory (OFAST) provides a method to achieve this goal.⁹¹ We performed OFAST calculations and found that the transition from the LL to HL structure was not thermodynamically favorable for any C₁–C₄ hydrocarbon at 35 °C. Details of these calculations are given in the Supporting Information. As a result of these observations, all of our simulations for hydrocarbon diffusion were performed in the LL ZIF-8 structure.

Figure 6 shows alkane and alkene self-diffusion coefficients as a function of fractional loading. Liquid-like loadings, θ_L , for all the alkanes and alkenes were computed from each species' bulk liquid density and the pore volume of ZIF-8, and they are tabulated in the Supporting Information. A higher loading of 22 molecules per cage was used for CH₄. This allowed us to include a loading at which the methane self-diffusion begins to

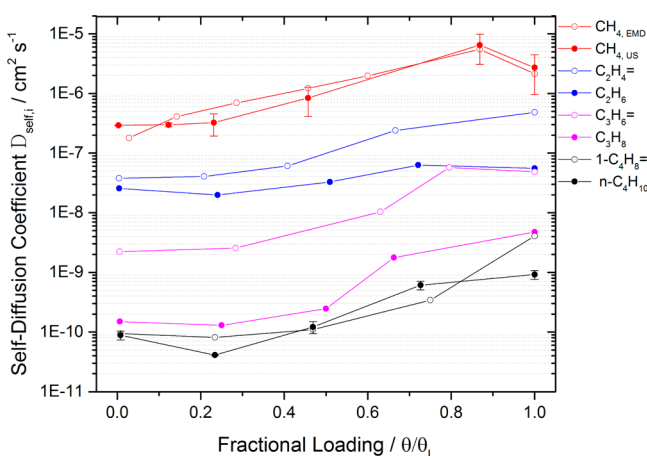


Figure 6. Short alkane and alkene self-diffusion coefficients as a function of unary fractional loading in ZIF-8 at 35 °C.

decrease due to steric hindrance in Figure 6. The CH₄ self-diffusivities computed with dcTST are fast enough that these quantities are also accessible from straightforward MD. The self-diffusivities of methane at 6 loadings were gathered using MD simulations during which self-diffusivities were computed using a computationally efficient order-*n* algorithm⁹² as well as with our dcTST method. These MD derived self-diffusion coefficients agree quantitatively with the dcTST derived self-diffusion coefficients at higher loadings, validating our accounting for only the hopping rates of symmetric cage loadings. dcTST also accurately predicts a decrease in the methane self-diffusivity at high loadings. The error bars on the methane and *n*-butane data in Figure 6 were generated by running 3 simulations at each loading, and we expect the uncertainties on all the other data in Figure 6 to be similar.

Over most of the fractional loading range, an increase in the self-diffusion coefficient is observed for all hydrocarbons. This behavior is attributed to a larger decrease in the free energy barrier of diffusion than the opposing decrease in the transmission coefficient due to adsorbate–adsorbate interactions. Examples of the free energy and transmission coefficient as a function of loading for propane are reported in the Supporting Information. Pusch and co-workers measured methane self-diffusivities in ZIF-8 using pulsed field gradient nuclear magnetic resonance (PFG NMR) over the loading range of 2.1 to 4.0 molec/cage, corresponding to bulk gas pressures of 7 and 14 bar, respectively.⁹³ Their results indicate a modest increase in the self-diffusivity from 8.8×10^{-11} to 1.4×10^{-10} m²/s over the reported loading range while our calculations predict methane self-diffusivities of 2.97×10^{-11} to 3.24×10^{-11} m²/s over a loading range of 2.7–5.1 molec/cage. Pantatosaki et al. reported a methane self-diffusion coefficient of 1.45×10^{-10} m²/s at a loading of 5.0 molec/cage using PFG NMR at 298 K⁹⁴ while we report a self-diffusion coefficient of 3.24×10^{-11} m²/s at the same loading. Jobic et al. measured methane self-diffusivities in ZIF-8 using quasi-electric neutron scattering (QENS) at 200 K and over a loading range of 0.5–7.0 molec/cage.⁹⁵ They extrapolated this data to 298 K with an activation energy of diffusion of 5 kJ/mol. At 200 and 298 K respectively, their reported self-diffusivities range from 2.7×10^{-11} to 1.6×10^{-10} m²/s (200 K) and 7.3×10^{-11} to 4.1×10^{-10} m²/s (298 K).

Zhang et al. reported methane self-diffusivities in ZIF-8 of 4.2×10^{-11} to 3.1×10^{-10} m²/s over a loading range of 0.3 to 12.5 molec/cage using a fully flexible NPT-MD simulations at 298 K.⁹⁶ We calculated methane self-diffusivities of 2.9×10^{-11} to 6.5×10^{-10} m²/s over a loading range of 0.1 to 19.0 molec/cage showing, as expected because they use the same force field, that our calculations are consistent with those of Zhang et al. Consistent with our finding that the free energy barrier for methane decreases by 11 kJ/mol over a loading of 5 to 19 molec/cage, they determined that the free energy barrier decreases by 10.3 kJ/mol over a loading range of 3 to 12.5 molec/cage.⁹⁶ Chmelik and co-workers measured ethane self-diffusivities of 8.81×10^{-12} to 9.14×10^{-12} m²/s in ZIF-8 at 298 K over a loading range of 0.2–3.7 molec/cage using infrared microscopy (IRM).^{97,98} Similarly, we observed almost constant ethane self-diffusion coefficients of 2.57×10^{-12} to 1.99×10^{-12} m²/s (the decrease observed is within the uncertainty of the dcTST calculations) over a loading range of 0.1–3.1 molec/cage. All comparisons of simulated to experimental self-diffusivities for C₁–C₂ hydrocarbons at higher

loadings in ZIF-8 are reported as figures in the [Supporting Information](#).

Figure 7 shows the alkane and alkene transport diffusivities in ZIF-8 as a function of fractional loading at 35 °C. These values

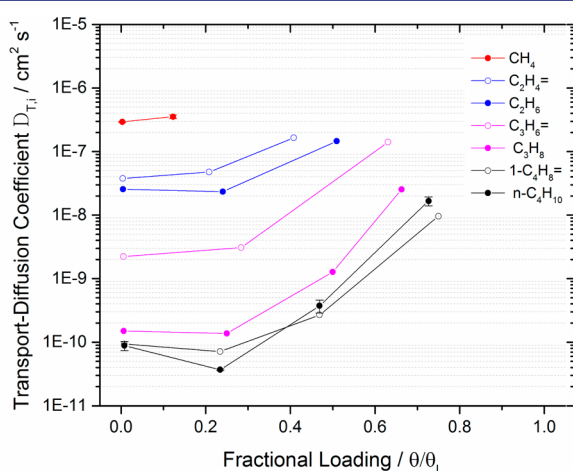


Figure 7. Short alkane and alkene transport diffusion coefficients as a function of unary fractional loading in ZIF-8 at 35 °C.

were calculated with eq 2 using the self-diffusivities in Figure 6 as well as GCMC derived adsorption isotherms of the hydrocarbons in ZIF-8. Very high fractional loadings were not included for several of the hydrocarbons since the isotherms were only calculated up to 10 bar. This cutoff pressure was arbitrarily chosen but is not without meaning. Having to compress a gas stream is costly, and a separation process operating at high pressures may be financially unattractive.

The transport diffusivities at finite loadings are greater than their self-diffusivity counterparts due to an increasing thermodynamic factor for all C1–C4 adsorbates. Chmelik and co-workers reported increasing unary methane transport diffusivities of 8.8×10^{-11} to 3.78×10^{-10} m²/s from infinite dilution to a loading of 2.1 methane molec/cage in ZIF-8 using IRM at 298 K.^{99–101} We observed a less sharp methane transport diffusivity increase of 2.93×10^{-11} to 3.54×10^{-11} m²/s over the loading range of 0.1–2.7 molec/cage. Pantatosaki et al. reported an increase in the methane transport diffusion in ZIF-8 of 3.70×10^{-10} to 1.62×10^{-9} m²/s over a loading range of 0.1–5.3 molec/cage using fully flexible NVT-MD simulations.⁹⁴ For these simulations, Pantatosaki et al. utilized the generic DREIDING FF and allowed for quasi-free motion of the 2-methylimidazolate linker. Bux et al. measured single-component ethylene and ethane transport diffusivities in ZIF-8 using IRM at 25 °C.^{19,99} For ethylene, they measured transport diffusivities of 4.97×10^{-11} to 6.68×10^{-10} m²/s in the loading range of 0.9–6.7 molec/cage while we report ethylene transport diffusivities of 3.79×10^{-12} to 1.64×10^{-11} m²/s in the loading range of 0.1–6.1 molec/cage. For ethane, they reported transport diffusivities of 1.11×10^{-11} to 1.48×10^{-10} m²/s in the loading range of 0.8–7.0 molec/cage while we calculated ethane transport diffusivities of 2.57×10^{-12} to 1.46×10^{-11} m²/s in the loading range of 0.1–6.6 molec/cage. They determined that the transport diffusivity is approximately constant for loadings of up to 4 molecules per cage, after which it increases rapidly for both adsorbates. We observe similar behavior, with both the ethylene and ethane simulated

transport diffusivities increasing sharply over a loading range of 3–6 molecules per cage. The order of magnitude disagreement between the simulated and experimental ethylene/ethane results may indicate lack of fidelity in the force fields used in our calculations, although further studies will be needed to clarify this issue.

Chmelik measured propylene and propane transport diffusion coefficients using IRM at 298 K,⁹⁹ and reported propylene transport diffusivities of 1.76×10^{-13} to 2.85×10^{-12} m²/s over a loading range of 0.4–4.9 molec/cage. We report propylene transport diffusivities of 2.22×10^{-13} to 1.41×10^{-11} m²/s over a loading range of 0.1–7 molec/cage, in very good agreement with Chmelik's data. For propane, Chmelik reported transport diffusivities of 4.86×10^{-16} to 2.48×10^{-15} over a loading range of 0.8 to 4.5 molec/cage. We reported propane diffusivities of 1.49×10^{-14} to 2.54×10^{-12} m²/s in the loading range of 0.1–6.6 molec/cage. Chmelik reports that a diffusion mediated mixing solvothermal synthesis procedure used to produce 300 μm ZIF-8 crystals yielded propane diffusivities closer to 10^{-14} m²/s but a conventional synthesis procedure¹⁰² yielding smaller ZIF-8 crystals produced the diffusivities reported above. The propylene diffusivities measured in both sets of crystals, however, were in agreement. Chmelik attributed the slow diffusion of propane in the nonconventionally synthesized materials to defects, although the reason that this did not similarly effect propylene diffusion is unclear. Zhang et al. reported a propane corrected transport diffusivity of 2.0×10^{-14} m²/s in 162 μm ZIF-8 crystals, measured using the pressure decay kinetic uptake method;¹³ our simulated values are in good agreement with this result. All comparisons of simulated to experimental transport diffusivities for C1–C3 hydrocarbons at higher loadings in ZIF-8 are reported as figures in the [Supporting Information](#).

4.3. ZIF-8 Membrane Property Predictions. With the above treatment of the transport diffusivities and the adsorption isotherms, it is possible to make direct comparisons to experimental permeance data for ZIF-8 membranes. This is motivated by recent advances in engineering nanoporous materials that act as the selective layer in membrane separations.^{103–105} Unary permeabilities were calculated numerically using the following relationship from Crank's derivation of concentration-dependent diffusion through a plane sheet:¹⁰⁶

$$P = \frac{J}{\Delta P/l} = \frac{1}{\Delta P} \int_{C_{\text{low}}}^{C_{\text{high}}} D_{T,i}(c) dc \quad (5)$$

where P is the permeability, J is the flux, l is the membrane thickness, ΔP is the transmembrane pressure drop, and $C_{\text{high}}(C_{\text{low}})$ is the concentration of the adsorbate at the feed (permeate) sides of the membrane. Figure 8 shows unary permeabilities of C1–C4 hydrocarbons as a function of feed pressure with a constant permeate pressure of 0 bar. Unary ZIF-8 membrane fluxes with respect to feed pressure are reported in the [Supporting Information](#) with an assumed membrane thickness of 1 μm. At pressures above 0.1 bar in Figure 8, an increase in the propylene and propane permeabilities is observed whereas a sharp decrease is observed in the 1-butene and *n*-butane permeabilities. According to GCMC-derived adsorption isotherms, near-saturation is observed at bulk pressures of ~0.4 bar for both 1-butene and *n*-butane. As the bulk pressure increases above ~0.4 bar, the loading, and correspondingly, the transport diffusion of the C4 hydrocarbons, does not change significantly. However,

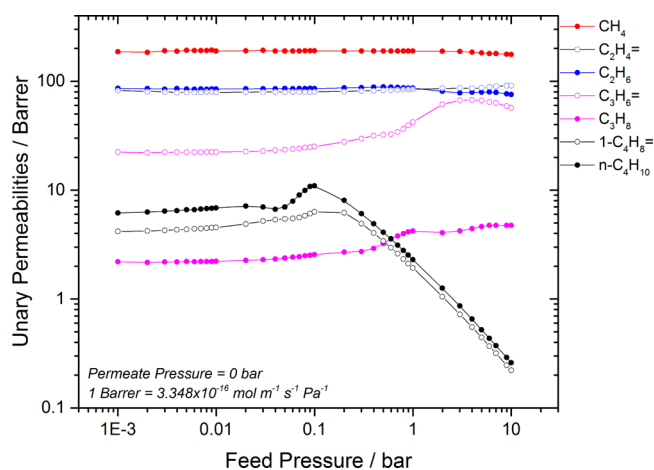


Figure 8. Short alkane and alkene permeabilities as a function of feed pressure in ZIF-8 at 35 °C.

according to eq 5, there is a penalty in the permeability from an increasing pressure drop across the ZIF-8 film. At bulk pressures between 1 and 10 bar, an increase in the permeability is observed for the C3 hydrocarbons since the transport diffusion coefficient increases under increased loadings in that pressure range. Pressures above 10 bar would provide a similar decrease in the C3 hydrocarbon permeabilities as that observed for the C4 hydrocarbons. At pressures below 1 bar, several qualitative features are observed. Ethane has a higher

permeability than ethylene through its stronger interaction with the ZIF-8 pore surface. This behavior is also observed for *n*-butane over both 1-butene and propane. Above 1 bar, however, we find that the order of permeabilities follows from the diffusion ranking (fastest to slowest): methane, ethylene, ethane, propylene, propane, *n*-butane/1-butene. The difference between the permeabilities of ethylene/ethane and *n*-butane/1-butene are within the uncertainty of the GCMC and MD calculations.

Table 1 shows permeability data from experiments with ZIF-8 membranes by Zhang et al.,¹³ Pan et al.,^{14,18,107} Brown et al.,¹⁰⁴ and Bux et al.^{19,20,102} along with simulated permeabilities at corresponding pressure drops and 35 °C. We have included studies that measured the permeances of at least 2 linear hydrocarbons. For each comparison, the limits of integration in eq 5 for the calculations were specifically set to match the experimentally reported feed and permeate bulk pressures. The four research groups noted here measured unary permeances using several different experimental methods: mixed matrix membrane permeation interpreted with a Maxwell model fitting, piezometric uptake rate measurement combined with adsorption isotherm data, the WK technique, and single gas permeation (SGP) with no sweep stream. Zhang et al. fabricated mixed matrix dense films containing 23.8 vol % ZIF-8 crystals and obtained permeabilities for C₁–C₃ hydrocarbons using the Maxwell model.¹³ They also reported permeabilities for C₃–C₄ hydrocarbons calculated using their measured corrected transport diffusivities and Langmuir isotherm fits to hydrocarbon adsorption data. Both methods

Table 1. Comparison of Simulated and Experimental Single-Component Hydrocarbon Permeabilities through ZIF-8 Membranes^a

adsorbate	author	technique	<i>l</i> (μm)/support	<i>T</i> (°C)	<i>P</i> _{Feed} (bar)	<i>P</i> _{Drop} (bar)	exp. <i>P</i> (Barrer)	sim. <i>P</i> (Barrer)
CH ₄	Zhang ¹³	M ³ P	–/M ² DF	35	2.0	2.0	270 ± 26	188
	Pan ¹⁸	WK	2.5/AD	23	1.01	1.01	576	189
	Pan ¹⁰⁷	WK	2/CHF	25	1.01	1.01	717 ± 60	189
	Bux ^{20,102}	WK	25/TA	25	1.00	1.00	567	189
	Bux ¹⁹	SGP	25/TA	20	6.0	5.0	1270	89
C ₂ H ₄ =	Zhang ¹³	M ³ P	–/M ² DF	35	2.0	2.0	1100 ± 500	85
	Pan ¹⁸	WK	2.5/AD	23	1.01	1.01	994	85
	Bux ¹⁹	SGP	25/TA	20	6.0	5.0	299	78
	Zhang ¹³	M ³ P	–/M ² DF	35	2.0	2.0	430 ± 130	81
C ₂ H ₆	Pan ¹⁸	WK	2.5/AD	23	1.01	1.01	503	87
	Pan ¹⁰⁷	WK	2/CHF	25	1.01	1.01	538 ± 30	87
	Zhang ¹³	M ³ P	–/M ² DF	35	2.0	2.0	210 ± 95	42
	Zhang ¹³	PURM·AI	–	35	2.0	2.0	390	42
C ₃ H ₆ =	Brown ¹⁰⁴	WK	8.8/THF	25	1.03	1.03	201.5	42
	Pan ¹⁸	WK	2.5/AD	23	1.01	1.01	77	42
	Zhang ¹³	M ³ P	–/M ² DF	35	2.0	2.0	2.5 ± 1.1	4
	Zhang ¹³	PURM·AI	–	35	2.0	2.0	2.9	4
C ₃ H ₈	Brown ¹⁰⁴	WK	8.8/THF	25	1.03	1.03	22.0	4
	Pan ¹⁸	WK	2.5/AD	23	1.01	1.01	5	4
	Pan ¹⁰⁷	WK	2/CHF	25	1.01	1.01	8 ± 1	4
	Zhang ¹³	PURM·AI	–	35	2.0	2.0	0.3	1
1-C ₄ H ₈ =	Zhang ¹³	PURM·AI	–	35	2.0	2.0	0.12	1
<i>n</i> -C ₄ H ₁₀	Zhang ¹³	PURM·AI	–	35	2.0	2.0	0.12	1
	Brown ¹⁰⁴	WK	8.8/THF	25	1.03	1.03	18.5	2
	Pan ¹⁸	WK	2.5/AD	25	1.01	1.01	4.0	2

^aSimulated permeabilities calculated at 35 °C with a transmembrane pressure drop corresponding to the experimental pressure drop. M³P = mixed matrix membrane permeation interpreted with a Maxwell Model; PURM·AI = piezometric uptake rate measurement combined with adsorption isotherm data; WK = Wicke–Kallenbach technique; SGP = single gas permeation; *T* = Torlon, C = ceramic + HF = hollow fiber; M²DF = mixed matrix dense film; TA = titania on an alumina support; AD = α-alumina discs; 1 Barrer = 3.348 × 10^{−16} mol m^{−1} s^{−1} Pa^{−1} = 10^{−10} cm³(STP)cm/(cm² s cmHg).

yielded similar $C_3=$ / C_3 permeabilities, validating their use of the Maxwell model. Brown et al. grew pure $8.8 \pm 1.4 \mu\text{m}$ ZIF-8 membranes on the bore side of Torlon hollow fibers and measured permeances for propylene, propane, and *n*-butane using the WK technique.¹⁰⁴ Pan et al. grew pure $2.5 \mu\text{m}$ thick ZIF-8 membranes on alumina discs and measured methane, ethylene, ethane, propylene, propane, and *n*-butane permeances with the WK technique with argon as a sweep gas.¹⁸ Pan et al. also performed a follow-up study in which they grew pure $\sim 2 \mu\text{m}$ thick ZIF-8 membranes on the outer surface of ceramic (yttria-stabilized zirconia) hollow fibers and measured methane, ethane, and propane permeances using the WK technique with argon at 1 bar as a sweep gas.¹⁰⁷ Bux et al. measured methane, ethylene and ethane unary permeances using SPG through a pure $25 \mu\text{m}$ thick ZIF-8 membrane on a alumina support covered by a smooth titania layer.^{19,20,102} Most of these studies have reported permeances at 20–25 °C (room temperature) but we have assumed that the comparison with our simulated 35 °C permeabilities are warranted.

On the whole, we find order of magnitude agreement between our simulated values and those reported experimentally. We report $C_2/C_3=$ (~ 2), and $C_3=$ / C_3 (~ 11) predicted ideal selectivities at a feed pressure of 1 bar, a transmembrane pressure drop of 1 bar, and a temperature of 35 °C. This behavior was previously known through experimental results, but for the first time has been demonstrated with simulations. Contrary to our findings, most experimental studies report higher ethylene permeabilities than methane permeabilities and similar methane/ethane permeabilities. Our results predict that methane has a higher permeability than both ethylene/ethane. Bux et al. reported an ideal permeance separation factor of 4.2 of ethylene over ethane at a feed pressure of 6 bar, transmembrane pressure drop of 5 bar, and temperature of 20 °C, whereas our simulated ideal permeance selectivity is 1.14. Comparison between the simulated and experimental adsorption isotherms reveals that the GCMC simulations underestimate both ethylene and ethane loading. Adsorbate-framework LJ interactions that more accurately reflect experimentally observed adsorption isotherms would likely improve our permeability predictions and possibly yield self-diffusivities in better agreement with experimental results. Such an investigation would be warranted but is outside the scope of this study.

In considering the data above, it is important to note that experimental permeance studies are also fraught with possible uncertainties. Experimental papers typically report permeances since it is difficult to measure membrane thicknesses accurately. However, for consistency in Table 1, we have multiplied their experimentally measured permeances by their reported membrane thicknesses as visually measured from cross-sectional SEM images. MOF membranes grown on support materials can contain a variety of defects such as missing linkers within the MOF film on the unit cell scale¹⁰⁸ and exposed support material (e.g., pinhole defects) leading to higher than expected fluxes.¹⁰⁹ While still an ongoing subject of research, it is also possible that different synthesis methods yield different chemical environments on the MOF film interfaces leading to non-negligible surface resistances.

5. CONCLUSIONS

We have computed the self-diffusivities of 15 adsorbates in flexible ZIF-8 as a function of temperature using dcTST and made extensive comparisons to reported experimental results.

These calculations include the diffusion of a much wider range of adsorbates than had previously been examined in ZIF-8 while incorporating the effects of framework flexibility. Our results show that it is possible to compute self-diffusivities using “off the shelf” force fields (FFs) with computationally efficient methods that allow diffusion that is much slower than can be probed with conventional MD. Our simulations show that large adsorbates brace open the window of ZIF-8, effectively rendering prior methodologies including empty framework flexibility unsuitable for the calculation of tight-fitting adsorbate diffusivities. This work is also the first to use dcTST to study the effect of finite loadings on hydrocarbon diffusion while maintaining full flexibility of the nanoporous framework. While we examined only unary loadings of hydrocarbons in ZIF-8, our methods can be extended to study multicomponent mixtures. The simulation techniques presented are well suited to predict MOF membrane properties in cage-type MOFs.

As is well-known, the quality of MD predictions relies heavily on the quality of the FF. The diffusion activation energy barrier in materials like ZIF-8 is an exponential function of window size⁴⁰ and as a result even small changes in the adsorbate–adsorbent FF parameters can yield order of magnitude differences in diffusivity values in some cases.^{20,40,94,96} In our calculations, we have used standard FFs without attempting to tune their properties in any way. These FFs appear to capture many features of adsorbate-framework interactions and framework flexibility effects accurately. The inability to directly compute diffusion coefficients for relevant molecules with previous methods, however, means that these FFs have not been parametrized with methods that generate high quality information for configurations near the transition state that are crucial to diffusion. Combining the simulation methods we have demonstrated in this paper with recent advances in deriving accurate adsorbate-framework FFs from DFT and other quantum chemistry calculations^{10,111} may create a useful means to improve on the FFs available for simulating adsorbate diffusion in MOFs.

■ ASSOCIATED CONTENT

📄 Supporting Information

The Supporting Information is available free of charge on the ACS Publications website at DOI: 10.1021/jacs.5b08746.

Details of the adsorbate FF parameters, additional dcTST simulation details, tables of free energy barriers, tables of calculated activated hopping rates, infinite dilution temperature dependent diffusivities, ZIF-8 window size distributions with all adsorbates, hydrocarbon adsorption isotherms, OFAST calculation details, tables of finite-loading self- and transport diffusivities, and calculated ZIF-8 membrane fluxes. (PDF)

■ AUTHOR INFORMATION

Corresponding Author

*david.sholl@chbe.gatech.edu

Notes

The authors declare the following competing financial interest(s): DSS holds an equity position in a company focused on production of MOFs.

■ ACKNOWLEDGMENTS

This work was supported by Phillips 66 Company. We acknowledge Jeffrey Camp, Dr. Jason Gee, Dr. Salah Boulfelfel, and Krishna Jayachandrababu for their insightful conversations.

■ REFERENCES

- (1) Eldridge, R. B. *Ind. Eng. Chem. Res.* **1993**, *32*, 2208–2212.
- (2) Van Miltenburg, A.; Zhu, W.; Kapteijn, F.; Moulijn, J. A. *Chem. Eng. Res. Des.* **2006**, *84*, 350–354.
- (3) Güciyener, C.; Gascon, J.; Kapteijn, F. In *Small-Scale Gas to Liquid Fuel Synthesis*; CRC Press: Boca Raton, FL, 2015; pp 135–188.
- (4) Zhou, H.-C.; Long, J. R.; Yaghi, O. M. *Chem. Rev.* **2012**, *112*, 673–674.
- (5) Lee, J.; Farha, O. K.; Roberts, J.; Scheidt, K. A.; Nguyen, S. T.; Hupp, J. T. *Chem. Soc. Rev.* **2009**, *38*, 1450–1459.
- (6) Kreno, L. E.; Leong, K.; Farha, O. K.; Allendorf, M.; Van Duyne, R. P.; Hupp, J. T. *Chem. Rev.* **2012**, *112*, 1105–1125.
- (7) Zhuang, J.; Kuo, C.-H.; Chou, L.-Y.; Liu, D.-Y.; Weerapana, E.; Tsung, C.-K. *ACS Nano* **2014**, *8*, 2812–2819.
- (8) Li, J.-R.; Sculley, J.; Zhou, H.-C. *Chem. Rev.* **2012**, *112*, 869–932.
- (9) Keskin, S.; Liu, J.; Rankin, R. B.; Johnson, J. K.; Sholl, D. S. *Ind. Eng. Chem. Res.* **2009**, *48*, 2355–2371.
- (10) Keskin, S.; van Heest, T. M.; Sholl, D. S. *ChemSusChem* **2010**, *3*, 879–891.
- (11) Chung, Y. G.; Camp, J.; Haranczyk, M.; Sikora, B. J.; Bury, W.; Krungleviciute, V.; Yildirim, T.; Farha, O. K.; Sholl, D. S.; Snurr, R. Q. *Chem. Mater.* **2014**, *26*, 6185–6192.
- (12) Park, K. S.; Ni, Z.; Côté, A. P.; Choi, J. Y.; Huang, R.; Uribe-Romo, F. J.; Chae, H. K.; O’Keeffe, M.; Yaghi, O. M. *Proc. Natl. Acad. Sci. U. S. A.* **2006**, *103*, 10186–10191.
- (13) Zhang, C.; Lively, R. P.; Zhang, K.; Johnson, J. R.; Karvan, O.; Koros, W. J. *J. Phys. Chem. Lett.* **2012**, *3*, 2130–2134.
- (14) Pan, Y.; Li, T.; Lestari, G.; Lai, Z. *J. Membr. Sci.* **2012**, *390*, 93–98.
- (15) Hara, N.; Yoshimune, M.; Negishi, H.; Haraya, K.; Hara, S.; Yamaguchi, T. *J. Membr. Sci.* **2014**, *450*, 215–223.
- (16) Kwon, H. T.; Jeong, H.-K. *J. Am. Chem. Soc.* **2013**, *135*, 10763–10768.
- (17) Liu, D.; Ma, X.; Xi, H.; Lin, Y. S. *J. Membr. Sci.* **2014**, *451*, 85–93.
- (18) Pan, Y.; Lai, Z. *Chem. Commun.* **2011**, *47*, 10275–10277.
- (19) Bux, H.; Chmelik, C.; Krishna, R.; Caro, J. *J. Membr. Sci.* **2011**, *369*, 284–289.
- (20) Hertäg, L.; Bux, H.; Caro, J.; Chmelik, C.; Remsungnen, T.; Knauth, M.; Fritzsche, S. *J. Membr. Sci.* **2011**, *377*, 36–41.
- (21) Parkes, M. V.; Demir, H.; Teich-McGoldrick, S. L.; Sholl, D. S.; Greathouse, J. A.; Allendorf, M. D. *Microporous Mesoporous Mater.* **2014**, *194*, 190–199.
- (22) Zheng, B.; Sant, M.; Demontis, P.; Suffritti, G. B. *J. Phys. Chem. C* **2012**, *116*, 933–938.
- (23) Gee, J. A.; Chung, J.; Nair, S.; Sholl, D. S. *J. Phys. Chem. C* **2013**, *117*, 3169–3176.
- (24) Sholl, D. S. *Acc. Chem. Res.* **2006**, *39*, 403–411.
- (25) Zheng, B.; Pan, Y.; Lai, Z.; Huang, K.-W. *Langmuir* **2013**, *29*, 8865–8872.
- (26) June, R. L.; Bell, A. T.; Theodorou, D. N. *J. Phys. Chem.* **1991**, *95*, 8866–8878.
- (27) Snurr, R. Q.; Bell, A. T.; Theodorou, D. N. *J. Phys. Chem.* **1994**, *98*, 11948–11961.
- (28) Auerbach, S. M.; Henson, N. J.; Cheetham, A. K.; Metiu, H. I. *J. Phys. Chem.* **1995**, *99*, 10600–10608.
- (29) Mosell, T.; Schrimpf, G.; Brickmann, J. *J. Phys. Chem.* **1996**, *100*, 4582–4590.
- (30) Maginn, E. J.; Bell, A. T.; Theodorou, D. N. *J. Phys. Chem.* **1996**, *100*, 7155–7173.
- (31) Mosell, T.; Schrimpf, G.; Brickmann, J. *J. Phys. Chem. B* **1997**, *101*, 9476–9484.
- (32) Mosell, T.; Schrimpf, G.; Brickmann, J. *J. Phys. Chem. B* **1997**, *101*, 9485–9494.
- (33) Forester, T. R.; Smith, W. J. *Chem. Soc., Faraday Trans.* **1997**, *93*, 3249–3257.
- (34) Jousse, F.; Auerbach, S. M. *J. Chem. Phys.* **1997**, *107*, 9629–9639.
- (35) Vlugt, T. J. H.; Dellago, C.; Smit, B. *J. Chem. Phys.* **2000**, *113*, 8791–8799.
- (36) Auerbach, S. M. *Int. Rev. Phys. Chem.* **2000**, *19*, 155–198.
- (37) Dubbeldam, D.; Beerdsen, E.; Vlugt, T. J. H.; Smit, B. *J. Chem. Phys.* **2005**, *122*, 224712.
- (38) Dubbeldam, D.; Beerdsen, E.; Calero, S.; Smit, B. *J. Phys. Chem. B* **2006**, *110*, 3164–3172.
- (39) Coudert, F. X.; Boutin, A.; Jeffroy, M.; Mellot-Draznieks, C.; Fuchs, A. H. *ChemPhysChem* **2011**, *12*, 247–258.
- (40) Haldoupis, E.; Watanabe, T.; Nair, S.; Sholl, D. S. *ChemPhysChem* **2012**, *13*, 3449–3452.
- (41) Watanabe, T.; Sholl, D. S. *Langmuir* **2012**, *28*, 14114–14128.
- (42) Fairen-Jimenez, D.; Moggach, S. A.; Wharmby, M. T.; Wright, P. A.; Parsons, S.; Düren, T. *J. Am. Chem. Soc.* **2011**, *133*, 8900–8902.
- (43) Zhang, K.; Lively, R. P.; Zhang, C.; Chance, R. R.; Koros, W. J.; Sholl, D. S.; Nair, S. *J. Phys. Chem. Lett.* **2013**, *4*, 3618–3622.
- (44) Peralta, D.; Chaplais, G.; Paillaud, J.-L.; Simon-Masseron, A.; Barthelet, K.; Pirngruber, G. D. *Microporous Mesoporous Mater.* **2013**, *173*, 1–5.
- (45) Skoulidas, A. I.; Sholl, D. S. *J. Phys. Chem. B* **2005**, *109*, 15760–15768.
- (46) Karger, J.; Binder, T.; Chmelik, C.; Hibbe, F.; Krautscheid, H.; Krishna, R.; Weitzkamp, J. *Nat. Mater.* **2014**, *13*, 333–343.
- (47) Haldoupis, E.; Nair, S.; Sholl, D. S. *J. Am. Chem. Soc.* **2010**, *132*, 7528–7539.
- (48) Frenkel, D.; Smit, B. *Understanding Molecular Simulation: From Algorithms to Applications*, 2nd ed.; Academic Press: New York, 2002.
- (49) Sholl, D. S.; Steckel, J. A. *Density Functional Theory: A Practical Introduction*; John Wiley & Sons, Inc.: Hoboken, NJ, 2009.
- (50) Henkelman, G.; Jonsson, H. *J. Chem. Phys.* **2000**, *113*, 9978–9985.
- (51) Torrie, G. M.; Valleau, J. P. *J. Comput. Phys.* **1977**, *23*, 187–199.
- (52) Kaestner, J. *Wiley Interdiscip. Rev. Comput. Mol. Sci.* **2011**, *1*, 932–942.
- (53) Voter, A. F.; Sørensen, M. R. In *MRS Proceedings: Symposium J.—Multiscale Modelling of Materials*; Bulatov, V. V., Diazde la Rubia, T., Phillips, R., Kaxiras, E., Ghoniem, N., Eds.; 1998; Vol. 538, pp 427–439.
- (54) Izrailev, S.; Stepaniants, S.; Isralewitz, B.; Kosztin, D.; Lu, H.; Molnar, F.; Wriggers, W.; Schulten, K. In *Computational Molecular Dynamics: Challenges, Methods, Ideas*; Springer: New York, 1999; pp 39–65.
- (55) Laio, A.; Parrinello, M. *Proc. Natl. Acad. Sci. U. S. A.* **2002**, *99*, 12562–12566.
- (56) Tunca, C.; Ford, D. M. *J. Chem. Phys.* **1999**, *111*, 2751–2760.
- (57) Dellago, C.; Bolhuis, P. G.; Csajka, F. S.; Chandler, D. *J. Chem. Phys.* **1998**, *108*, 1964–1977.
- (58) van Erp, T. S.; Bolhuis, P. G. *J. Comput. Phys.* **2005**, *205*, 157–181.
- (59) Kirkwood, J. G. *J. Chem. Phys.* **1935**, *3*, 300–313.
- (60) Abouelnasr, M. K. F.; Smit, B. *Phys. Chem. Chem. Phys.* **2012**, *14*, 11600–11609.
- (61) Voter, A. F.; Doll, J. D. *J. Chem. Phys.* **1985**, *82*, 80–92.
- (62) Awati, R. V.; Ravikovitch, P. I.; Sholl, D. S. *J. Phys. Chem. C* **2013**, *117*, 13462–13473.
- (63) Awati, R. V.; Ravikovitch, P. I.; Sholl, D. S. *J. Phys. Chem. C* **2015**, *119*, 16596–16605.
- (64) Boulfelfel, S.; Ravikovitch, P. I.; Sholl, D. S. *J. Phys. Chem. C* **2015**, *119*, 15643–15653.
- (65) Tunca, C.; Ford, D. M. *Chem. Eng. Sci.* **2003**, *58*, 3373–3383.
- (66) Tunca, C.; Ford, D. M. *J. Phys. Chem. B* **2002**, *106*, 10982–10990.

- (67) Beerdsen, E.; Dubbeldam, D.; Smit, B. *J. Phys. Chem. B* **2006**, *110*, 22754–22772.
- (68) Jee, S. E.; Sholl, D. S. *J. Am. Chem. Soc.* **2009**, *131*, 7896–7904.
- (69) Kolokathis, P. D.; Pantatosaki, E.; Gatsiou, C.-A.; Jobic, H.; Papadopoulos, G. K.; Theodorou, D. N. *Mol. Simul.* **2014**, *40*, 80–100.
- (70) Zhang, L.; Hu, Z.; Jiang, J. *J. Am. Chem. Soc.* **2013**, *135*, 3722–3728.
- (71) Allen, F. *Acta Crystallogr., Sect. B: Struct. Sci.* **2002**, *58*, 380–388.
- (72) Wu, H.; Zhou, W.; Yildirim, T. *J. Am. Chem. Soc.* **2007**, *129*, 5314–5315.
- (73) Martin, M. G.; Siepmann, J. I. *J. Phys. Chem. B* **1998**, *102*, 2569–2577.
- (74) Wick, C. D.; Martin, M. G.; Siepmann, J. I. *J. Phys. Chem. B* **2000**, *104*, 8008–8016.
- (75) Dubbeldam, D.; Calero, S.; Vlucht, T. J. H.; Krishna, R.; Maesen, T. L. M.; Smit, B. *J. Phys. Chem. B* **2004**, *108*, 12301–12313.
- (76) Talu, O.; Myers, A. L. *AIChE J.* **2001**, *47*, 1160–1168.
- (77) Clark, L. A.; Gupta, A.; Snurr, R. Q. *J. Phys. Chem. B* **1998**, *102*, 6720–6731.
- (78) Brand, S. K.; Colón, Y. J.; Getman, R. B.; Snurr, R. Q. *Microporous Mesoporous Mater.* **2013**, *171*, 103–109.
- (79) Potoff, J. J.; Siepmann, J. I. *AIChE J.* **2001**, *47*, 1676–1682.
- (80) Zhang, L.; Siepmann, J. I. *Theor. Chem. Acc.* **2006**, *115*, 391–397.
- (81) Harris, J. G.; Yung, K. H. *J. Phys. Chem.* **1995**, *99*, 12021–12024.
- (82) Dubbeldam, D.; Calero, S.; Ellis, D. E.; Snurr, R. Q. *Mol. Simul.* **2016**, *42*, 1–21.
- (83) Plimpton, S. J. *Comput. Phys.* **1995**, *117*, 1–19.
- (84) Fiorin, G.; Klein, M. L.; Hénin, J. *Mol. Phys.* **2013**, *111*, 3345–3362.
- (85) Grossfield, A. *WHAM: The Weighted Histogram Analysis Method*, version 2.0.9; Department of Biochemistry and Biophysics, University of Rochester Medical Center: Rochester, NY, 2013; <http://membrane.urmc.rochester.edu/content/wham>.
- (86) Eum, K.; Jayachandrababu, K. C.; Rashidi, F.; Zhang, K.; Leisen, J.; Graham, S.; Lively, R. P.; Chance, R. R.; Sholl, D. S.; Jones, C. W.; Nair, S. *J. Am. Chem. Soc.* **2015**, *137*, 4191.
- (87) Willems, T. F.; Rycroft, C. H.; Kazi, M.; Meza, J. C.; Haranczyk, M. *Microporous Mesoporous Mater.* **2012**, *149*, 134–141.
- (88) Corma, A.; Rey, F.; Rius, J.; Sabater, M. J.; Valencia, S. *Nature* **2004**, *431*, 287–290.
- (89) Newman, M. E. J.; Ziff, R. M. *Phys. Rev. E: Stat. Phys., Plasmas, Fluids, Relat. Interdiscip. Top.* **2001**, *64*, 016706.
- (90) Fairen-Jimenez, D.; Galvelis, R.; Torrisi, A.; Gellan, A. D.; Wharmby, M. T.; Wright, P. A.; Mellot-Draznieks, C.; Duren, T. *Dalton Trans.* **2012**, *41*, 10752–10762.
- (91) Coudert, F.-X.; Jeffroy, M.; Fuchs, A. H.; Boutin, A.; Mellot-Draznieks, C. *J. Am. Chem. Soc.* **2008**, *130*, 14294–14302.
- (92) Dubbeldam, D.; Ford, D. C.; Ellis, D. E.; Snurr, R. Q. *Mol. Simul.* **2009**, *35*, 1084–1097.
- (93) Pusch, A.-K.; Splith, T.; Moschkowitz, L.; Karmakar, S.; Biniwale, R.; Sant, M.; Suffritti, G.; Demontis, P.; Cravillon, J.; Pantatosaki, E.; Stallmach, F. *Adsorption* **2012**, *18*, 359–366.
- (94) Pantatosaki, E.; Megariotis, G.; Pusch, A.-K.; Chmelik, C.; Stallmach, F.; Papadopoulos, G. K. *J. Phys. Chem. C* **2012**, *116*, 201–207.
- (95) Jobic, H.; Kolokolov, D. I.; Stepanov, A. G.; Koza, M. M.; Ollivier, J. *J. Phys. Chem. C* **2015**, *119*, 16115–16120.
- (96) Zhang, L.; Wu, G.; Jiang, J. *J. Phys. Chem. C* **2014**, *118*, 8788–8794.
- (97) Chmelik, C.; Bux, H.; Caro, J.; Heinke, L.; Hibbe, F.; Titze, T.; Kärger, J. *Phys. Rev. Lett.* **2010**, *104*, 085902.
- (98) Chmelik, C.; Freude, D.; Bux, H.; Haase, J. *Microporous Mesoporous Mater.* **2012**, *147*, 135–141.
- (99) Chmelik, C. *Microporous Mesoporous Mater.* **2015**, *216*, 138–145.
- (100) Chmelik, C.; van Baten, J.; Krishna, R. *J. Membr. Sci.* **2012**, *397–398*, 87–91.
- (101) Bux, H.; Chmelik, C.; van Baten, J. M.; Krishna, R.; Caro, J. *Adv. Mater.* **2010**, *22*, 4741–4743.
- (102) Bux, H.; Liang, F.; Li, Y.; Cravillon, J.; Wiebcke, M.; Caro, J. *J. Am. Chem. Soc.* **2009**, *131*, 16000–16001.
- (103) Koros, W. J. *AIChE J.* **2004**, *50*, 2326–2334.
- (104) Brown, A. J.; Brunelli, N. A.; Eum, K.; Rashidi, F.; Johnson, J. R.; Koros, W. J.; Jones, C. W.; Nair, S. *Science* **2014**, *345*, 72–75.
- (105) Brown, A. J.; Johnson, J. R.; Lydon, M. E.; Koros, W. J.; Jones, C. W.; Nair, S. *Angew. Chem., Int. Ed.* **2012**, *51*, 10615–10618.
- (106) Crank, J. *The Mathematics of Diffusion*; Oxford University Press: New York, 1979.
- (107) Pan, Y.; Wang, B.; Lai, Z. *J. Membr. Sci.* **2012**, *421–422*, 292–298.
- (108) Sholl, D. S. *Nat. Chem.* **2011**, *3*, 429–430.
- (109) Koros, W. J.; Fleming, G. K. *J. Membr. Sci.* **1993**, *83*, 1–80.
- (110) Kulkarni, A.; Sholl, D. S. *Langmuir* **2015**, *31*, 8453–8468.
- (111) Fang, H.; Demir, H.; Kamakoti, P.; Sholl, D. S. *J. Mater. Chem. A* **2014**, *2*, 274–291.